Electrical Manipulation of Crystal Symmetry for Switching Transverse Acoustic Phonons

H. Jeong,[1] Y. D. Jho,[1,*] and C. J. Stanton[2]
[1]School of Information and Communications, Gwangju Institute of Science and Technology, Gwangju 500-712, Korea
[2]Department of Physics, University of Florida, Gainesville, Florida 32611, USA
(Received 21 July 2014; published 29 January 2015)

We experimentally explore the use of a novel device where lateral electric fields can be applied to break the translational symmetry within the isotropic plane and hence change the selection rules to allow normally forbidden transverse acoustic (TA) phonon generations. The ultrafast screening of the lateral electric field by the photocarriers relieves shear strain in the structure and switches on the propagating TA waves. The amplitude and on-state time of the TA mode can be modulated by the external field strength and size of the laterally biased region. The observed frequency shift with an external bias as well as the strong geometrical dependence confirm the role of the asymmetric potential distribution in electrically manipulating the crystal symmetry to control modal behavior of acoustic phonons.

DOI: 10.1103/PhysRevLett.114.043603 PACS numbers: 42.50.Wk, 63.20.-e, 78.20.hc, 78.35.+c

The ability to tailor materials and device elements below the phonon mean free path in such a way that the vibrational or phononic properties can be modified and precisely controlled has gained widespread interest in recent years [1]. Some applications include controllability of the thermal conductivity for on-chip heat management [2,3], charge transfer via acoustic (AC) pulses [4], thermoelectric power generation [5,6], the realization of phonon cavities [7–9], and lasers [10,11]. The acoustic counterparts of diodes [12] and metamaterials [13] open further opportunities for the prospective development of phononics.

The coherent vibrational properties can typically be investigated using transient coupling between electrons and dynamic strains under femtosecond laser excitation. Such techniques have been reported for multiferroic crystals [14], zinc-blende crystals [15], wurtzite semiconductors [16,17], and their mixtures [18]. In the viewpoint of phononic manipulations, crystal orientation has predetermined the AC mode selection in most of the previous studies; in the anisotropic plane, transverse acoustic (TA) and longitudinal acoustic (LA) phonons are simultaneously observed, whereas in isotropic systems, only the LA mode generation is allowed. For manipulating the crystal symmetry, strains were often imposed by using lattice-mismatch-induced axial stresses [19,20]. On the other hand, the role of vertical electric fields and electronic transport alongside the growth axis in generating optical phonons [21] and AC phonons [16,22–24] has been identified.

By positing the growth direction as the decisive factor fixing the phonon modes in the previous efforts, however, it has remained challenging to *externally* manipulate the phononic properties such as selection rules for modal generation, propagation velocities, and acoustic birefringence. To meet this need, in this Letter, we employ a novel and practical approach of electrical symmetry manipulation, which can be formulated in terms of electrically selected strains and strain-induced perturbations on the elastic and dielectric tensors, to attain an unprecedented degree of freedom in the switchability of the forbidden TA mode in an isotropic wurtzite system.

A representative sample used here under asymmetric potential distribution at room temperature is illustrated in Fig. 1(a). GaN-based multiple quantum wells (MQWs) acting as LA epicenters [16] were sandwiched between p and n regions along the c axis ($\equiv z$ axis) so that the external bias V_{ext} induces vertically exerted fields compensating for the piezoelectric field E_z^P [25]. The fundamental importance of the structure lies in the additional formation of *lateral* electric fields between interdigitated contact pads; the sample has narrow p and n electrodes, which are laterally spaced by $\sim$80 μm in the x direction on top of an abnormally thin indium tin oxide (ITO) layer ($\sim$40 nm) to spread a nonuniform electric current density along the x axis. The following layers were sequentially grown on a sapphire substrate by metal-organic chemical vapor deposition: 3-μm-thick undoped GaN, 2.5-μm-thick n-GaN, six quantum well (QW) layers of 2-nm-thick $In_{0.1}Ga_{0.9}N$ encased by seven 8-nm-thick GaN barriers, 120-nm-thick p-$Al_{0.05}Ga_{0.95}N$, and 250-nm-thick p-GaN. The doped electron n_e and hole concentrations n_p were estimated to be 7×10^{17} and 8×10^{17} cm^{-3}, respectively.

To determine the potential distributions in both the vertical and lateral directions, the spatially resolved photoluminescence (PL) was measured, as shown in Fig. 1(b), under excitation by a frequency-doubled Ti:sapphire laser at 367.5 nm onto a spot size of $\sim$10 μm. As the excitation spot was moved away from the p electrode in the lateral x direction in Fig. 1(b), the PL peak energy was redshifted when V_{ext} was applied. The redshift of the PL peak energy, which was distinctive from those reported for vertically strained QWs, indicates that the actual magnitude of the applied bias along the z axis differed from V_{ext} and

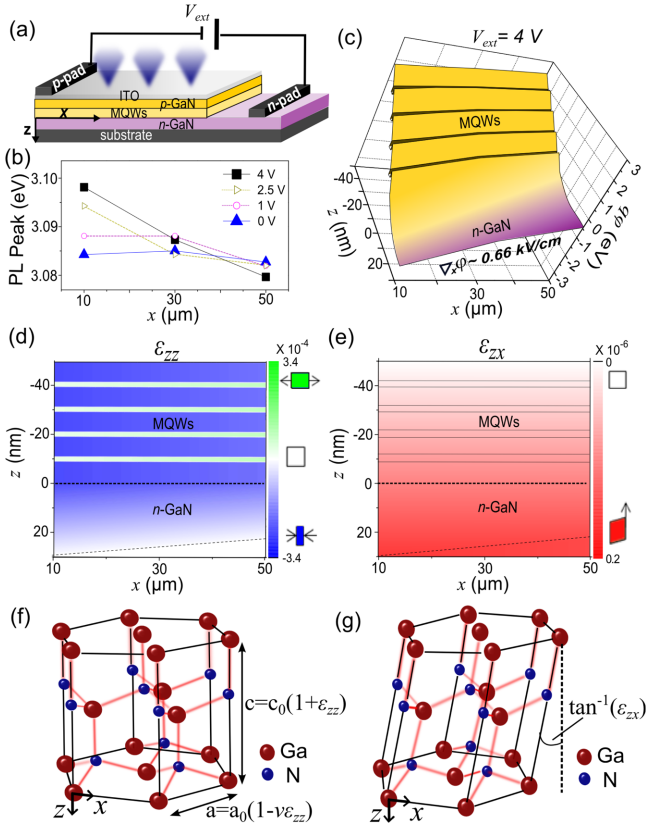

FIG. 1 (color online). (a) Schematic of a structure with asymmetry potential distribution; blue cones denote laser excitation spots moving along the x axis (from p contact to n contact). (b) PL peak energy as a function of excitation position in the lateral (x) direction under external bias (V_{ext}). (c) Conduction band profile near the MQW/n-GaN interface calculated from the PL peak energy variations at 4 V. Spatial distributions of (d) normal strain ε_{zz} and (e) shear strain ε_{zx} deduced from the conduction band profile. Lattice structures distorted by (f) ε_{zz} and (g) ε_{zx}, where ν is the Poisson's ratio.

decreased along the x axis in terms of the quantum-confined Stark effect [25]. From variational calculations of the PL peak energy, we estimated E_z^P to be 0.98 MV/cm and determined the laterally varying potential profile $\varphi(x,z)$. The resultant $\varphi(x,z)$ in the conduction band was evaluated in Fig. 1(c) at a V_{ext} of 4 V across the MQW and n-depletion regions. Then, the lateral electric field $E_x = -\nabla_x\varphi$ was found to increase with V_{ext}, reaching ~0.66 kV/cm at 4 V at the end of the depletion region. In Fig. 1(c), E_z^P was almost fully compensated at 4 V by the vertically applied fields; the magnitude of the net electric field along the z axis $E_z = -\nabla_z\varphi$ was on the same order as E_x within the QWs.

On the basis of the piezoelectric tensor d_{nm}, the strain components in hexagonal symmetry in wurtzite GaN are coupled with the electric field distributions as $\varepsilon_m = \sum_{n=1}^{3} d_{nm}E_n$ $(m = 1, 2, \ldots, 6)$ [26], where nonzero values of $E_3 = E_z$ and $E_1 = E_x$ lead to the normal ($\varepsilon_{zz} = \varepsilon_3$) and shear strain components ($\varepsilon_{zx} = \varepsilon_5$) in the x-z plane, respectively. The normal strain ε_{zz} calculated in Fig. 1(d) was compressive in the barriers and weakly tensile in the QWs at 4 V. On the other hand, the shear component (ε_{zx}) in Fig. 1(e) became prominent throughout the biased region and reached a maximum value near the end of the n-depletion region.

The strain-induced structural distortions are shown schematically in Figs. 1(f) and 1(g). The volumetric deformation in Fig. 1(f), where the lattice constants are modulated as $c = c_0(1 + \varepsilon_{zz})$ and $a = a_0(1 - \nu\varepsilon_{zz})$ from the original undeformed values of c_0 and a_0, implies that the structure is still laterally isotropic. Whereas in the monoclinic distortion of Fig. 1(g), the shear strain ε_{zx} is geometrically defined as an angular change to tilt the c axis by $\tan^{-1}(\varepsilon_{zx})$ [26], breaking the optical and mechanical symmetry in the c plane [27]. When the rapid screening of the directional electric fields relieves the strains in the distorted structures and displacively initiates propagating coherent AC phonons, the driving force in the loaded string model [17,24] is now extended in a correlated manner with the electrically selected strains as

$$S_i(x,z,t) = \frac{1}{\rho_0}\bar{C}_i\varepsilon_i(x,z)H(t), \tag{1}$$

where the mode index i corresponds to either LA or TA, $\bar{C}_i$ is the effective elastic constants [27], ε_{LA} (ε_{TA}) corresponds to the normal (shear) strain ε_{zz} (ε_{zx}), and $H(t)$ is the Heaviside step function describing the instantaneous excitation of the driving forces by transient field screenings.

To investigate the interplay between the asymmetric potential distribution and the modal AC phonon dynamics, we measured the time-resolved differential reflectivity spectra (DRS) as sketched in Fig. 2(a). The fluence of the pump beam was ~85 μJ/cm^2 in order to abruptly screen out the potential gradients. The incident angle θ of the pump beam for phonon generation was fixed at 0, whereas θ for the polarized probe beam for phonon detection was set to less than 5°. For photocarrier excitation in the MQW and depletion regions, the pump and probe beam energies were degenerate at 367.5 nm, with a penetration depth ξ of around 700 nm. The probe polarization ϕ was fixed at 45° with respect to the incident plane except in Fig. 4, whereas the pump beam was polarized perpendicular to the probe beam.

The temporal changes in DRS in Fig. 2(b), representing the recombination and transport dynamics of photocarriers in the strained QWs [25], superimposed the oscillatory components which were subsequently extracted in Fig. 2(c) in the time domain and in Fig. 2(d) in the spectrum domain. Two distinct frequency modes of the oscillations were caused by dynamic Fabry-Perot interference between the probe beams reflected from the surface and from the wave front of the propagating strain waves. The modal frequency is expressed as $f_i = 2v_i n\cos(\theta_t)/\lambda_{\text{probe}}$, where θ_t is the

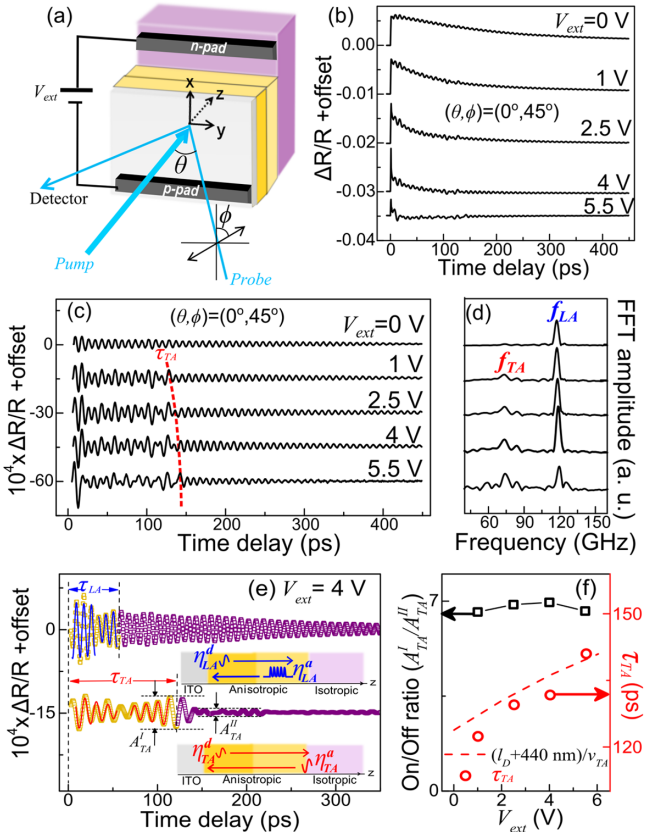

FIG. 2 (color online). (a) Measurement schematic for DRS due to AC phonons. (b) Transient DRS as a function of time delay under different V_{ext} from 0 to 5.5 V. (c) Oscillatory parts of DRS due to acoustic phonons. (d) Fast Fourier transform (FFT) spectra of the acoustic phonon signals. (e) Band-pass-filtered signals under 4 V around the LA (108–144 GHz) and TA (52–88 GHz) modes. Insets outline the epicenters and propagation of the AC modes. (f) On/off amplitude ratio of the TA wave and on-state time τ_{TA} as a function of V_{ext}.

angle of the probe transmission inside the material, n is the refractive index, and λ_{probe} is the wavelength of the probe beam. Not only does the LA frequency f_{LA} ~120 GHz but also the spectral component at $f_{\mathrm{TA}} \sim 70$ GHz, newly emergent with V_{ext}. Further, f_{LA} (f_{TA}) matches well the velocity v_{LA} (v_{TA}) of ~7300 m/s (4200 m/s) [27]. The actively induced TA mode under a nonzero V_{ext} could not be explained by any previous investigations of the isotropic plane. Furthermore, the TA waves abruptly disappeared around τ_{TA} (~130 ps at 4 V), which is indicated by a curved dashed line in Fig. 2(c). The sideband components of the TA mode in Fig. 2(d) could be associated with the drastic decay of TA signals in Fig. 2(c) around τ_{TA}; on the other hand, the LA mode also showed the sidebands above 4 V at which the electronic tunneling in a time scale of $\sim 2/f_{\mathrm{LA}}$ led to the accelerated decay of the LA mode.

The detailed line-shape analysis in Fig. 2(e) further revealed that the band-pass-filtered TA and LA signals (scattered lines) could be matched with the solid fitting curves by adaptively integrating the product of the sensitivity function F_i [24] and the strain η_i; i.e., $\Delta R/R = \int_{-\infty}^{\infty} dz F_i e^{-z/\xi} \eta_i$, where η_i is the linear supposition between descending waves (η_i^d, which propagate toward the substrate and represent decaying signals for $0 < t < \tau_i/2$) and ascending waves (η_i^a, which propagate toward the surface and represent growing signals for $\tau_i/2 < t < \tau_i$). By taking the time scale in the biased region ($\tau_{\mathrm{LA}} \sim 55$ ps and $\tau_{\mathrm{TA}} \sim 130$ ps at 4 V) into account, both η^d_{TA} and η^d_{LA} were determined to spatially originate from the middle of the surface depletion region (SDR), whereas η^a_{TA} and η^a_{LA} were found to have different epicenters, in the n-depletion and MQW regions, respectively. These spatially concentrated AC strains, therefore, could be simplified into $\eta_i^a = \int_{D_i^a} \varepsilon_i(z) dz \delta(z + v_i t)$ for the ascending waves and $\eta_i^d = \int_{D_i^d} \varepsilon_i(z) dz \delta(z - v_i t)$ for the descending waves, where the region of integration D_i^d (D_i^a) corresponds to the SDR (either to the MQW region for the LA mode or to the n-depletion region for the TA mode).

The on/off ratio of the TA mode $A^I_{\mathrm{TA}}/A^{II}_{\mathrm{TA}}$ was held at ~7 with an external bias in Fig. 2(f), where A^I_{TA} (A^{II}_{TA}) corresponds to the maximum TA amplitude for the on state (off state) for time domain I (II) with $t < \tau_i$ ($\tau_i < t < 2\tau_i$). This is explained by the estimated AC reflectivity of about 0.19 due to the AC impedance mismatch at the ITO/p-GaN interface. The increasing on-state time τ_{TA} (red circles) in Fig. 2(f), on the other hand, was in good agreement with the calculated travel time (dashed line) between the end of the n-depletion region and the SDR. In this regard, the slightly increased value of τ_{TA} between 2.5 and 5.5 V (~11 ps) can be converted into the elongated n-depletion region width $l_D(n_e, n_p, V_{\mathrm{ext}})$ [25]. It was previously postulated that the dielectric tensor modulation due to transient shear strain waves can be detected only with oblique probe incidence in an optically isotropic medium [46]. Therefore, the digitized appearance of the TA mode even under normal incidence in Fig. 2, which matches exactly the time of flight in the laterally biased region, implies that the hexagonal symmetry was broken for τ_{TA}.

To precisely trace the frequencies and amplitudes without phase-change-induced errors at the AC interfaces [27], the Fourier amplitudes for η_i^a integrated over $\tau_i/2 < t < \tau_i$ are presented for the TA (red lines) and LA (blue lines) modes at different V_{ext} in Fig. 3(a). Different behaviors of the signal amplitudes with respect to bias are contrasted in Fig. 3(b). The TA amplitude increased consistently with shear strain even beyond 4 V, at which electronic tunneling overrides the ε_{zz} increment and causes a relative decrease in the photocarrier screening within QWs, on the order of the exciton Bohr radius a_B, which is known to play a major role in LA mode generation [17]. However, this fast electronic transport could not weaken the TA amplification in Figs. 3(a) and 3(b), which suggests a distinctive origin

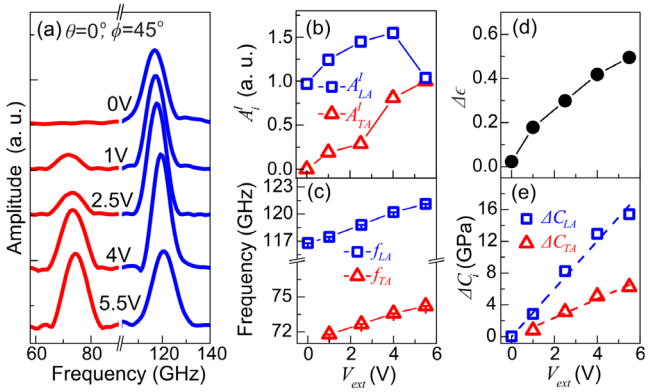

FIG. 3 (color online). (a) Modal spectra for ascending waves as a function of V_{ext}. (b) AC mode amplitudes with increasing V_{ext}. (c) Peak frequency for each AC mode under V_{ext}. (d) V_{ext}-induced variation in dielectric constant. (e) V_{ext}-induced elastic constant variation for each mode.

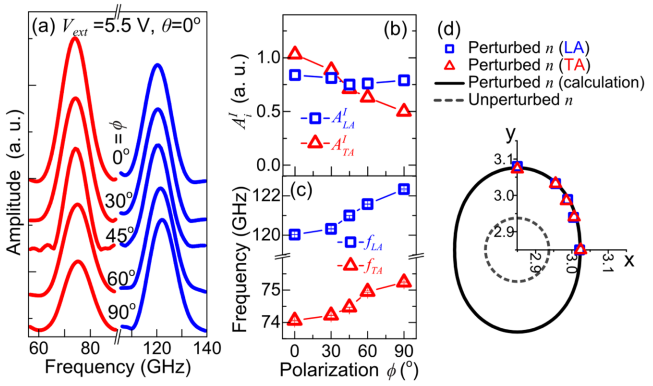

FIG. 4 (color online). (a) Modal spectra for ascending waves at different probe polarizations ϕ under V_{ext} of 5.5 V. (b) AC mode amplitudes with ϕ from 0° to 90°. (c) Peak frequency for each AC mode as a function of ϕ. (d) Refractive index ellipsoids for perturbed (at 5.5 V) and unperturbed (at 0 V) structures.

of TA mode generation at a much larger scale than a_B. Another intriguing feature regarding the electrically broken symmetry was the spectral blueshift in both modes under increasing V_{ext} in Fig. 3(a). The peak frequencies of the LA and TA modes increased with the bias by ~1.7%, as traced in Fig. 3(c). In terms of the birefringence in the anisotropic region, we first examined the V_{ext}-dependent refractive index change $n = \sqrt{\epsilon^o + \Delta\epsilon(V_{\text{ext}})}$ by incorporating ellipsometry results in Fig. 3(d). The unperturbed dielectric constant ϵ^o was evaluated to be 8.64 at 367.5 nm at zero bias. Then, inserting the measured n into f_i under V_{ext}, we extracted v_i, given by $v_i = \sqrt{(C_i + \Delta C_i(V_{\text{ext}})/\rho_0)}$. The additional bias-dependent changes $\Delta\epsilon(V_{\text{ext}})$ and $\Delta C_i(V_{\text{ext}})$ presented in Figs. 3(d) and 3(e) were further compared with the analytical expressions as $\Delta\epsilon \simeq p_{13}e_{33}E_z + \frac{1}{2}(p_{13} + p_{15})e_{15}E_x$, $\Delta C_{\text{LA}} \simeq C^H_{333}e_{33}E_z + ((C^M_{355})^2/(C^0_{33} - C^0_{44}))e^2_{15}E^2_x$, and $\Delta C_{\text{TA}} \simeq C^H_{443}e_{33}E_z - ((C^M_{355})^2/(C^0_{33} - C^0_{44}))e^2_{15}E^2_x$ through the optical birefringence and strain-induced nonlinear elasticity in the anisotropic region [27], where p_{ij} is the photoelastic tensor component, C^H_{lmn} (C^M_{lmn}) is the third-order elastic (TOE) coefficient for the normal (shear) strain, and C^0_{33} (C^0_{44}) is the unperturbed elastic constant for the LA (TA) mode. We also note that from a degeneracy perspective, TA modes could be further classified according to the atomic displacements parallel to either the x axis or the y axis (corresponding modal velocities, indexed by $v_{\text{TA}\|x}$ or $v_{\text{TA}\|y}$ [27]) and experimentally characterized if E_y had been available in our structures, which can be discussed elsewhere under the scope of the acoustic birefringence.

Regarding the electrically manipulated crystal symmetry, E_x distorted the hexagonal symmetry via the TOE tensors into monoclinic symmetry as illustrated in Fig. 1(g). Concretely, the tilting of the principal axis away from the c axis by E_x-induced monoclinic deformation, quantified by $\tan^{-1}(\varepsilon_{zx})$, could also be confirmed by angular perturbations of the elastic constants and refractive index in the x-y plane. Figure 4(a) shows the modal spectra at a V_{ext} of 5.5 V, integrated over $\tau_i/2 < t < \tau_i$, as we rotate the probe polarization ϕ from the x axis. Two noteworthy observations were made. (1) In clear contrast to the constant LA mode (blue lines), the TA amplitude (red lines) monotonically decreased with ϕ in Fig. 4(a), indicating that the TA mode was partially polarized along the same direction as E_x. Indeed, the TA magnitude (A^I_{TA}) in Fig. 4(b) revealed a drastic decrease by about 50%. (2) Despite the fixed V_{ext}, the modal frequencies f_{LA} and f_{TA} exhibited very similar increases with ϕ, as shown in Fig. 4(c), owing to the birefringence in the anisotropic region. As a function of ϕ, in this regard, n was extracted either from f_{LA} (blue squares) or from f_{TA} (red triangles) in Fig. 4(d). The dashed inner circle in Fig. 4(d) displays the isotropic refractive index ellipsoid without E_x, whereas the solid outer circle exhibits the values calculated via the E_x-induced optical birefringence which relatively reduced n along the x axis about −0.04. In a comparative structure without E_x even under an applied V_{ext}, where the TOE tensor has preserved hexagonal symmetry, this V_{ext}-induced birefringence and nonlinear elasticity vanished [27].

In summary, we reported the switchable generation of coherent TA waves in wurtzite heterostructures grown along the symmetry axis. By applying lateral electric fields in the isotropic plane, we could modify the selection rules, allowing the generation of the forbidden TA mode even under the normal incidence. Owing to the anisotropic nature of the elastic tensor over the laterally biased scale, the amplitude, velocity, and on-state times of the TA waves were also externally controlled. Finally, this work could pave the way toward practical applications where vibrational modes can be controlled electrically. Furthermore, as the electric fields couple strongly to the phonons in piezoelectric nanostructures, as demonstrated in this Letter, the activation of phononic functionalities with a degree of

control analogous to that for manipulating electrons in transistors could be heralded as the essential step in advancing integrated phononic circuits for logical processing.

We acknowledge useful discussions with P. Ruello, P. Grünberg, and K. J. Yee. This work was funded by Samsung Electronics (SRFC-IT1402-07).

*jho@gist.ac.kr

[1] See, e.g., M. Maldovan, Nature (London) **503**, 209 (2013).
[2] J.-K. Yu, S. Mitrovic, D. Tham, J. Varghese, and J. R. Heath, Nat. Nanotechnol. **5**, 718 (2010).
[3] R. Venkatasubramanian, E. Siivola, T. Colpitts, and B. O'Quinn, Nature (London) **413**, 597 (2001).
[4] E. S. K. Young, A. V. Akimov, M. Henini, L. Eaves, and A. J. Kent, Phys. Rev. Lett. **108**, 226601 (2012).
[5] G. J. Snyder and E. S. Toberer, Nat. Mater. **7**, 105 (2008).
[6] K. Biswas, J. He, I. D. Blum, C.-I. Wu, T. P. Hogan, D. N. Seidman, V. P. Dravid, and M. G. Kanatzidis, Nature (London) **489**, 414 (2012).
[7] M. Trigo, A. Bruchhausen, A. Fainstein, B. Jusserand, and V. Thierry-Mieg, Phys. Rev. Lett. **89**, 227402 (2002).
[8] A. Huynh, N. D. Lanzillotti-Kimura, B. Jusserand, B. Perrin, A. Fainstein, M. F. Pascual-Winter, E. Peronne, and A. Lemaître, Phys. Rev. Lett. **97**, 115502 (2006).
[9] G. Rozas, M. F. Pascual Winter, B. Jusserand, A. Fainstein, B. Perrin, E. Semenova, and A. Lemaître, Phys. Rev. Lett. **102**, 015502 (2009).
[10] See, e.g., A. Fainstein, N. D. Lanzillotti-Kimura, B. Jusserand, and B. Perrin, Phys. Rev. Lett. **110**, 037403 (2013).
[11] I. Mahboob, K. Nishiguchi, A. Fujiwara, and H. Yamaguchi, Phys. Rev. Lett. **110**, 127202 (2013).
[12] X.-F. Li, X. Ni, L. Feng, M. H. Lu, C. He, and Y. F. Chen, Phys. Rev. Lett. **106**, 084301 (2011).
[13] S. Guenneau, A. Movchan, G. Pétursson, and S. A. Ramakrishna, New J. Phys. **9**, 399 (2007).
[14] M. Lejman, G. Vaudel, I. C. Infante, V. E. Gusev, B. Dkhil, and P. Ruello, Nat. Commun. **5**, 5301 (2014).
[15] O. Matsuda, O. B. Wright, D. H. Hurley, V. E. Gusev, and K. Shimizu, Phys. Rev. Lett. **93**, 095501 (2004).
[16] K. H. Lin, C. M. Lai, C. C. Pan, J. I. Chyi, J. W. Shi, S. Z. Sun, C. F. Chang, and C.-K. Sun, Nat. Nanotechnol. **2**, 704 (2007).
[17] G.-W. Chern, C.-K. Sun, G. D. Sanders, and C. J. Stanton, Top. Appl. Phys. **92**, 339 (2004).
[18] O. Matsuda, O. B. Wright, D. H. Hurley, V. E. Gusev, and K. Shimizu, Phys. Rev. B **77**, 224110 (2008).
[19] V. Darakchieva, T. Paskova, M. Schubert, H. Arwin, P. P. Paskov, B. Monemar, D. Hommel, M. Heuken, J. Off, F. Scholz, B. A. Haskell, P. T. Fini, J. S. Speck, and S. Nakamura, Phys. Rev. B **75**, 195217 (2007).
[20] V. Darakchieva, P. P. Paskov, T. Paskova, E. Valcheva, B. Monemar, and M. Heuken, Appl. Phys. Lett. **82**, 703 (2003).
[21] T. Dekorsy, G. C. Cho, and H. Kurz, in *Light Scattering in Solids VIII*, edited by M. Cardona and G. Güntherodt (Springer, Berlin, 2000), Vol. 76, p. 169.
[22] C.-C. Chen, H.-M. Huang, T.-C. Lu, H.-C. Kuo, and C.-K. Sun, Appl. Phys. Lett. **100**, 201905 (2012).
[23] C. S. Kim, J. H. Kim, H. Jeong, Y. D. Jho, H. K. Kwon, H. S. Lee, J. S. Park, K. Song, S. H. Kim, Y. J. Kim, D. Lee, and K. J. Yee, Appl. Phys. Lett. **100**, 101105 (2012).
[24] R. Liu, G. D. Sanders, C. J. Stanton, C. S. Kim, J. S. Yahng, Y. D. Jho, K. J. Yee, E. Oh, and D. S. Kim, Phys. Rev. B **72**, 195335 (2005).
[25] Y. D. Jho, J. S. Yahng, E. Oh, and D. S. Kim, Phys. Rev. B **66**, 035334 (2002).
[26] J. F. Nye, *Physical Properties of Crystals* (Oxford University Press, Oxford, England, 1985).
[27] See Supplemental Material at http://link.aps.org/supplemental/10.1103/PhysRevLett.114.043603, which includes Refs. [28–45], for the formalisms on the strain-dependent model of AC phonon generation and electrical modulation of elastic and dielectric tensors, together with the detailed experimental results regarding the excitation fluence dependence, line-shape analysis, and lateral-electric-field-induced mechanical and optical anisotropy.
[28] G. Yu, G. Wang, H. Ishikawa, M. Umeno, T. Soga, T. Egawa, J. Watanabe, and T. Jimbo, Appl. Phys. Lett. **70**, 3209 (1997).
[29] Y.-C. Wen, T.-S. Ko, T.-C. Lu, H.-C. Kuo, J.-I. Chyi, and C.-K. Sun, Phys. Rev. B **80**, 195201 (2009).
[30] C.-T. Yu, K.-H. Lin, C.-L. Hsieh, C.-C. Pan, J.-I. Chyi, and C.-K. Sun, Appl. Phys. Lett. **87**, 093114 (2005).
[31] U. Jahn, S. Dhar, M. Ramsteiner, and K. Fujiwara, Phys. Rev. B **69**, 115323 (2004).
[32] A. S. Barker, Jr., and M. Ilegems, Phys. Rev. B **7**, 743 (1973).
[33] M. Wraback, H. Shen, J. C. Carrano, T. Li, J. C. Campbell, M. J. Schurman, and I. T. Ferguson, Appl. Phys. Lett. **76**, 1155 (2000).
[34] K.-H. Lin, G.-W. Chern, S.-W. Chu, C.-K. Sun, H. Xing, Y. Smorchkova, S. Keller, U. Mishra, and S. P. DenBaars, Appl. Phys. Lett. **81**, 3975 (2002).
[35] K.-H. Lin, C.-T. Yu, Y.-C. Wen, and C.-K. Sun, Appl. Phys. Lett. **86**, 093110 (2005).
[36] M. Foussekis, A. A. Baski, and M. A. Reshchikov, Appl. Phys. Lett. **94**, 162116 (2009).
[37] A. Polian, M. Grimsditch, and I. Grzegory, J. Appl. Phys. **79**, 3343 (1996).
[38] T. Wittkowski, J. Jorzick, H. Seitz, B. Schröder, K. Jung, and B. Hillebrands, Thin Solid Films **398–399**, 465 (2001).
[39] M. R. Armstrong, E. J. Reed, K.-Y. Kim, J. H. Glownia, W. M. Howard, E. L. Piner, and J. C. Roberts, Nat. Phys. **5**, 285 (2009).
[40] *Sensing with Terahertz Radiation*, edited by D. Mittleman (Springer, New York, 2003).
[41] Y.-C. Wen, S.-H. Guol, H.-P. Chen, J.-K. Sheu, and C.-K. Sun, Appl. Phys. Lett. **99**, 051913 (2011).
[42] C. J. Stanton, G. D. Sanders, R. Liu, G.-W. Chern, C.-K. Sun, J. S. Yang, Y. D. Jho, J. Y. Sohn, E. Oh, and D. S. Kim, Superlattices Microstruct. **34**, 525 (2003).
[43] B. O. Seraphin and N. Bottka, Phys. Rev. **139**, A560 (1965).
[44] F. Stern, Phys. Rev. **133**, A1653 (1964).
[45] R. F. Fuck and I. Tsvankin, Geophysics **74**, WB79 (2009).
[46] O. Matsuda and O. B. Wright, Anal. Sci. **17**, S216 (2001).